AIAA AVIATION Forum
12-16 June 2023, San Diego, CA and Online
AIAA AVIATION 2023 Forum

10.2514/6.2023-3213

Wavelet-based Analysis of Spectral and Temporal Structures in F404 Engine Jet Noise

Tyce W. Olaveson[1] and Kent L. Gee[2]
Brigham Young University, Provo, Utah, 84602, USA

Jon Paul Johnson[3]
Brigham Young University-Idaho, Rexburg, Idaho, 83440, USA

Spatiospectral lobes are features identified in the noise fields radiated from full-scale tactical aircraft that are unseen in lab-scale experiments. Prior studies have explored lobe frequency-domain characteristics, but a joint time-frequency domain (JTFD) analysis has the potential to further explore these phenomena and connect them to source-related events. This paper applies an event-based beamforming technique to acoustical data collected at a 120-microphone array near a T-7A-installed F404 engine. The algorithm correlates time domain events between pairs of adjacent microphones to find an event propagation direction and then ray traces to the jet centerline to identify an apparent source location. A wavelet transform is used to identify frequency triggers tied to the spatiospectral lobes to gain insights. It is shown that the source responsible for the spatiospectral lobes is composed of multiple, overlapping sources each with a different peak radiation angle. Events are also observed in the time-frequency domain, and it is found that there is an underlying temporal structure reminiscent of mode switching seen with lab-scale jet screech. Using a Markov-style analysis, this temporal structure is characterized. It is found that spectral peaks related to the spatiospectral lobes are composed of discrete but randomly distributed temporospectral events, each with a frequency-dependent directivity.

I. Nomenclature

AB	=	Afterburner
c	=	Sound speed
D_j	=	Fully expanded jet diameter
EBBF	=	Event-based beamforming
MIL	=	Military power
Sr	=	Strouhal number
T	=	Markov transition matrix
τ	=	Cross correlation time delay
θ	=	Event propagation angle
W_x	=	Wavelet transform of signal x
$\lvert W_x \rvert^2$	=	Wavelet power spectrum
x_e	=	event lipline location

II. Introduction

High-performance military jet aircraft are known to produce intense sound levels. Repeated exposure to these sound fields can lead to hearing loss [1]. Additionally, sound fields predicted by numerical simulations and lab-scale measurements do not completely agree with those of full-scale tactical aircraft in terms of phenomena produced. For

[1] Graduate Student, Brigham Young University, AIAA student member
[2] Professor, Department of Physics and Astronomy, AIAA Associate Fellow.
[3] Professor, Department of Physics and Astronomy.

this reason, it is desirable to characterize the noise generated by full-scale aircraft to further inform noise reduction efforts.

A key feature of full-scale high-performance military aircraft is the presence of multiple spatiospectral lobes. These lobes were formally identified by Wall et al. [2,3]. In their analysis of high-performance military jet aircraft noise, acoustical holography was used to create total-field reconstructions, and the lobes were characterized as distinct regions of high sound level that evolved through frequency. Before this work, the lobes were identified as a "dual-peak" phenomenon at individual microphone locations [4–6], in part because of limited spatial resolution and one-third octave band spectral analyses. The spatiospectral lobes can also be retroactively seen in other analyses. For example, Stout et al. [7] performed an intensity analysis in the near field of a high-performance aircraft. In their vector intensity plots and attached multimedia, multiple lobes can be seen to form with increasing frequency and evolve spatially.

The methods used to study these lobes have taken many forms. Harker et al. [5] performed preliminary correlation and coherence analysis where they suggested that the dual-peaked spectra were created by multiple overlapping and incoherent sources in the jet. These conclusions were later expanded on by Swift et al. [8] who performed a similar analysis on a different aircraft. In their work, at least five individual spatiospectral lobes were identified. It was shown that coherence lengths increase within an individual lobe and decrease in regions of overlap between two or more lobes. Beyond these standard signal processing techniques on the field-acquired data, inverse methods such as beamforming and holography have recently been largely employed to explore the apparent origin of and other spatial behavior of the lobes. Wall et al. [3] used near-field acoustical holography (NAH) to recreate the sound field near a high-performance military aircraft. They then employed a partial field decomposition method to separate the lobes and showed that two of the lobes are the product of overlapping partial sources. Leete et al. [9] used multisource statistically optimized near-field acoustical holography (M-SONAH) to track the lobes through space and frequency for the F-35. They determined that as frequency increases the lobes shift aft and eventually decrease in level while the next lobe appears at a steeper angle. This behavior can also be seen in the vector intensity analysis of Stout et al. [7,10]. These results were also confirmed by Olaveson et al. [11] using the hybrid beamforming method [12] to generate total-field reconstructions from T-7A noise data. In their analysis, they used a ray tracing technique to determine the apparent source locations of each lobe. Using SONAH, Mathews et al. [13] created noise-field reconstructions at the nozzle lipline. In conjunction with LES and previous analysis, they suggested that lipline source locations corresponding to the spatiospectral lobes coincide with the potential and supersonic core tips.

All the above methods, except correlation, operate in the frequency domain and the spectral averaging procedure inherent in these analyses removes any temporal features. However, to better understand the underlying mechanisms of the lobes, it is important to observe the waveform temporal features. One time domain analysis that is frequently used in jet noise analysis is Schlieren imaging. This method uses snapshots of density fluctuations to visualize acoustic radiation. This has seen repeated use in Mach wave analysis [14,15] where directivities can be identified from evenly spaced wavefronts. However, this methodology is largely confined to lab-scale jets due to the required imaging components. An alternative computational time-domain analysis has been developed in the form of event-based beamforming by Vaughn et al. [16–18]. In their crackle studies, they identified high amplitude and high derivative events in the time waveform and used a cross-correlation to beamform these events back to the jet lipline. The selected events and resultant distributions helped identify radiation and source characteristics of Mach waves and other known jet noise structures.

While each domain provides its unique insights, a joint time-frequency domain (JTFD) analysis has the potential of connecting features from both domains. The wavelet transform is a method of extracting frequency information at every time step in a signal [19], and has proven useful in identifying frequency events that change rapidly through time. Wavelet-based JTFD analysis has been seen in geophysical applications [19], shock noise identification [20], screech mode identification [21], and Mach wave reconstruction in conjunction with Schlieren imaging [15].

In this paper, the near-field noise generated by a T-7A-installed F404 engine is analyzed. The event-based beamforming algorithm is used in conjunction with the wavelet transform to further characterize the spatiospectral lobes in terms of their time event properties. The time-frequency structure of the wavelet is then explored to identify any transient structures and evidence is provided for a temporal shifting that is potentially similar to that seen in jets with mode switching present. A Markov-style probability analysis is then used to characterize the underlying structure. It is found that events in the wavelet transform corresponding to different spectral peaks are more likely to occur at different times with relatively few instances of overlap.

III. Experiment

On August 18th, 2019 at Holloman Air Force Base, data were collected from an F404 engine installed on a T-7A trainer aircraft [22]. The aircraft was tethered to the ground and performed six run-ups, each cycling through power settings ranging from idle to afterburner (AB) including military power (MIL). The endeavor featured multiple sets of near-field arrays and far-field arcs with a microphone array reference point (MARP) at 3.96 m downstream of the nozzle. Overall, there were over 200 microphones. For this paper, only the 120-microphone, near-field imaging array is used. This array was composed of GRAS 46BD and 46BG ¼" pressure mics sampling at 204.8 kHz. Figure 1 shows a schematic of the imaging array setup. The array ran approximately parallel to the jet centerline in the forward direction and then transitioned to follow the anticipated shear layer downstream of the nozzle. A variable microphone spacing was chosen to best capture the expected peak frequency behavior in each region.

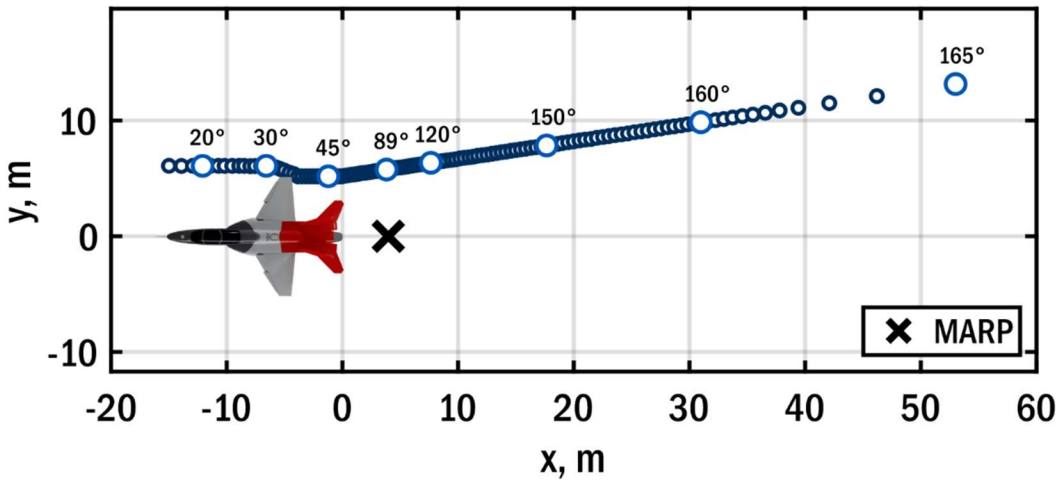

Figure 1. Schematic of the T-7A measurement.

The spectra from the recorded data at MIL power were computed and compiled into a spatiospectral plot. Figure 2 shows the top 6 dB of the plot with a 3 dB-down contour in white. The limited dynamic range has been selected to emphasize the spatiospectral lobe behavior. At least five spatiospectral lobes can be observed in this figure, with the first occurring just below a Strouhal number of 0.1 and above 24 D_j. The higher-ordered lobes (2+) appear as dark patches near Strouhal numbers of 0.15, 0.24, 0.31, and 0.39 respectively. This paper only analyses military power because the lobes are clearest at this engine condition.

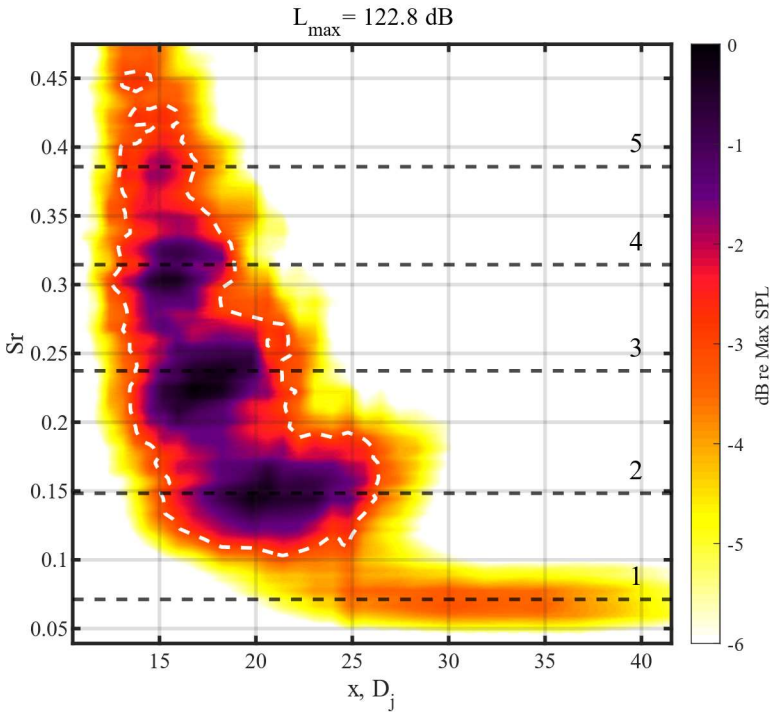

Figure 2. Spatiospectral plot for the T-7A at MIL engine condition. The figure shows Strouhal number as a function of microphone position. Note that the series of dark patches are spatiospectral lobes. The white contour identifies the 3dB down point.

IV. Methods

This section provides an overview of the methods used in this paper. The event-based beamforming (EBBF) method used by Vaughn et al. [23] is reviewed followed by a description of the wavelet transform.

A. Event-based beamforming

The goal of the EBBF procedure is to identify apparent locations and propagation angles of specified time domain events. In their study on crackle, Vaughn et al. [18,23] investigated both high-amplitude and large derivative events, but ultimately chose the latter as the large derivatives had been previously correlated with perceived crackle [24,25]. However, whatever event trigger is chosen, the EBBF process is the same.

For each pair of adjacent microphones, events are identified in the upstream microphone. For high amplitude or high derivative events, the event identification is as straightforward as locating local maxima in the pressure or derivative pressure waveform. More complicated events, such as a specific waveshape, can be identified using a cross-correlation but these have not yet been explored. Once events have been identified, the top 500 most prominent events are selected with a minimum of 2.4 ms separation between each event. The separation is included to both prevent events from being double counted as well as to ensure a broader sampling of the waveform.

For each event, a 20 ms Hann window is applied to the waveform, centered on the event. A similar window is also applied to the upstream microphone. This process isolates the event in each waveform. The cross correlation between the two waveforms is then calculated, from which a time delay is determined by taking the time lag, τ, at the maximum correlation coefficient. Using this time delay, a sound speed of $c = 343$ m/s, and the assumption that the event is locally planar in the region of the microphones, the apparent propagation angle and source location is reduced to a geometry problem.

Figure 3 shows the geometry assumed in EBBF. The vector $\overrightarrow{r_m}$ points from the upstream to the downstream microphone and has a length equal to the distance between the two, though the length has been exaggerated. The vector $\overrightarrow{r_s}$ is points from the microphone midpoint to the jet lipline and represents the apparent event path. The path is assumed to bisect the microphones so that the locally planar assumption holds. Following the same formulation as Vaughn et al. [18], the event propagation angle is then determined as:

$$\theta = 180° - (\phi + \alpha), \tag{1}$$

where $\alpha = tan^{-1}\left(\frac{\Delta y}{\Delta x}\right)$ is the angle formed from the microphone geometry and $\phi = cos^{-1}\left(\frac{c\tau}{d}\right)$ is the intersection angle between the microphone array and the event propagation path. Assuming a straight ray propagation path, the apparent event location is then extracted from the definition of the dot product:

$$\overrightarrow{r_m} \cdot \overrightarrow{r_s} = |\overrightarrow{r_m}||\overrightarrow{r_s}|\cos\phi. \tag{2}$$

For purposes of this paper, the event is assumed to come from the lipline location $\langle x_e, D_j/2, h\rangle$ where h is the height of the center of the nozzle. Thus, every component of $\overrightarrow{r_s}$ is known except for the x component which contains the information about the apparent event origin. Now Eq. 2 can be solved for the apparent event lipline location, x_e, by breaking each vector into components. This ray-tracing procedure is performed for each of the 500 events to allow for statistical analysis of the events.

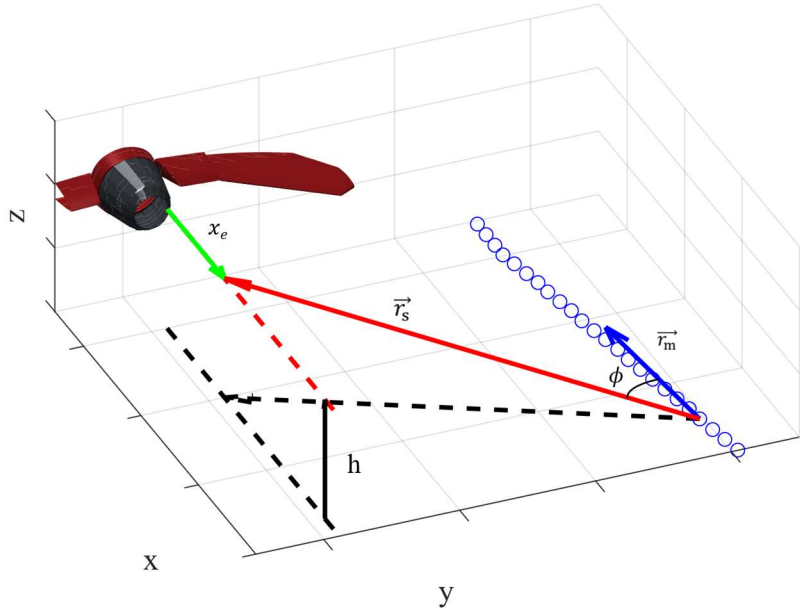

Figure 3. Geometry of the event-based beamforming approach. Microphones are represented by blue circles and other features of interest are indicated by arrows. The angle of incidence ϕ is calculated from the cross-correlation and events are propagated back to the jet lipline along the vector $\overrightarrow{r_s}$. The apparent lipline location is then calculated as x_e.

B. Wavelet Transform

Whereas the prior EBBF procedure was developed purely for the time domain, examining the spatiospectral lobe behavior in detail also requires frequency information as a function of time. The short-time Fourier transform can provide this information, but the uncertainty principle dictates that increasing the time resolution by decreasing data block size also decreases the frequency resolution [26]. A balance between the two can be attempted, but the EBBF algorithm requires a very high time resolution. Even with time steps of 20 ms, the errors of propagation angle and lipline intercept surpass what is reasonable. Thus, a different method is required.

The wavelet transform is a method of extracting frequency information at every instant in time [19]. The basic formulation involves repeatedly convolving a time signal, x, with a wavelet, Ψ, that is scaled to match a specific frequency of interest. In this paper, the Morlet wavelet is used, though other wavelet choices are being explored. The output of the transform is the complex function $W_x = W_x(Sr, t)$. From here the magnitude and phase information can be analyzed individually [15]; it is also beneficial to define the wavelet power spectrum, $|W_x|^2$ [19]. When viewed in

this way the result is a scalogram that depicts frequency-dependent energy content through time. Figure 4 shows an example 50 ms waveform (top) and the corresponding wavelet power spectrum (bottom). The selected waveform contains crackle as evidenced by the shocks. These shocks appear in $|W_x|^2$ as faint vertical stripes of high-Strouhal number content at the shock location [27]. In addition to the shock events, there are two large, high-amplitude islands or blobs at relatively low Strouhal numbers: 15 ms at $\mathrm{Sr} = 0.24$ and 27 ms at $\mathrm{Sr} = 0.15$. These Stouhal numbers represent prominent peaks seen in the time-averaged spectrum. The temporal structure of the events at these Strouhal numbers will be characterized further in Section V.B.

By taking time slices of $|W_x|^2$, i.e., $|W_x(Sr_t, t)|^2$ the amplitude of a target Strouhal number, Sr_t, is tracked through time. These time slices are then individually passed into the EBBF algorithm where large amplitudes are used as the event trigger. This identifies spatial characteristics corresponding to portions of the initial waveform with a relatively large amount of energy at the target Strouhal numbers.

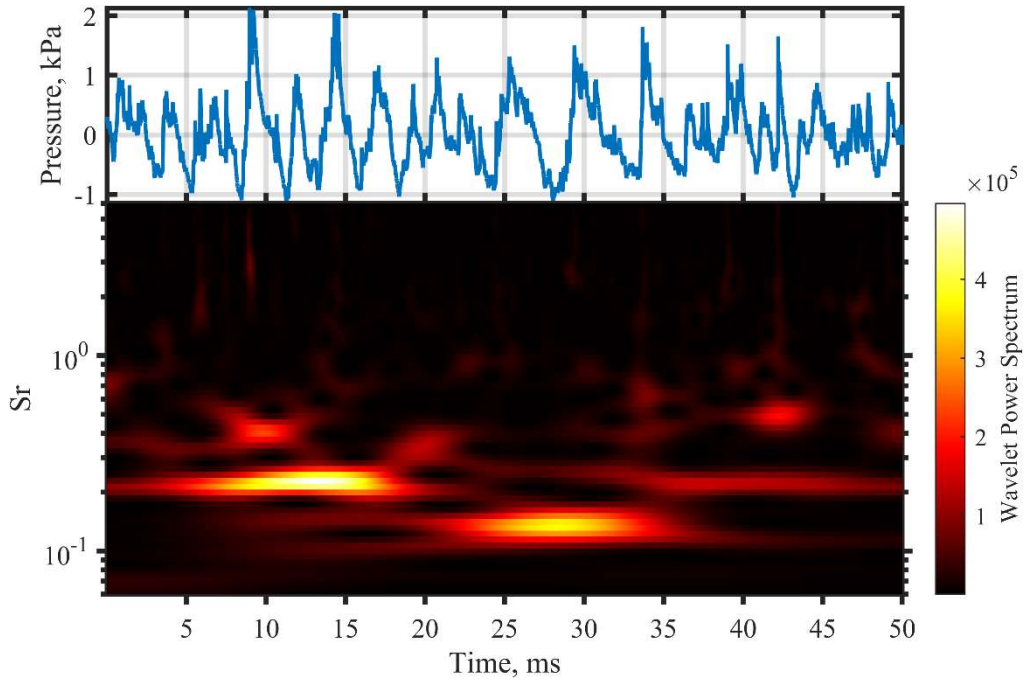

Figure 4. A 50 ms waveform sample and the corresponding wavelet power spectrum. The two bright islands at 15 ms and 27 ms indicate spectral events in the original waveform at these times. The corresponding Strouhal numbers, 0.15 and 0.24, are related to the peaks seen in the time-averaged spectrum.

V. Analysis

This section applies the wavelet transform to EBBF to target Strouhal numbers corresponding to the spatiospectral lobes. Statistical results are discussed concerning the predicted lobe directivities and source location. The temporal structure of events in the wavelet transform is then characterized using a Markov chain. Finally, the time-averaged spectrum is decomposed based on events in the wavelet transform.

A. Event-Based Beamforming with Wavelets

Whereas EBBF has been used to characterize crackle-related events, the purpose of this paper is to explore temporal characteristics of the spatiospectral lobes. To do this, slices of constant Strouhal number are extracted from $|W_x|^2$ and used in EBBF using maximum-amplitude events. This translates to beamforming at locations where the signal has a relatively large amount of energy at the desired Strouhal number. Whereas Vaughn et al. [23] suggested using the top 1000 events, in this paper only 500 events are used. When the wavelet transform is used to extract the amplitude of a single frequency, many of the temporal peaks from the original waveform vanish; thus, there are often fewer than 1000 notable events in each frequency slice which may introduce non-physical results.

Since only a subset of the imaging array shows evidence of the spatiospectral lobes, only the affected range of microphones will be used in the beamforming. Using Fig. 2 as a guide, the relative spatiospectral regions are presented in Table 1. While the spectral characteristics of the lobes shift with position, only a single Strouhal number is chosen

to characterize the lobes. This is because the wavelet-based EBBF can only target a single Strouhal number at a time. The ranges presented here are generous enough to capture the 3dB-down point around each. The propagation angles and apparent lipline source locations for each collection of events are compiled into normalized histograms to better visualize the data.

Lobe	Strouhal number	Spatial range
1	0.07	$24D_j \leq x \leq 39D_j$
2	0.15	$15D_j \leq x \leq 26D_j$
3	0.24	$13D_j \leq x \leq 21D_j$
4	0.31	$13D_j \leq x \leq 17D_j$
5	0.39	$13D_j \leq x \leq 17D_j$

Table 1. Spatiospectral regions corresponding to each lobe seen in Fig. 2.

Figure 5 shows the angle and intercept histograms as a function of microphone location for each of the spatiospectral lobes. The probability of each event is calculated as the number of events that fall into that bin, divided by the total number of events. These probabilities are indicated by color with values below 0.01 set to white to better see the relevant trends. Note that for the higher-ordered lobes, especially lobes 4 and 5, there are relatively few microphones within the lobe's spatial extent, thus these figures appear slightly blurred.

Initial observations of the propagation angle plots (top) indicate that the events responsible for each of the lobes have a relatively steady propagation angle albeit with a slight upward trend with increasing microphone position. These slight upward trends say that events must propagate at steeper angles to reach the farther microphones. This implies that the sources responsible for these events remain relatively constant. This is confirmed by inspection of the intercept plots (bottom).

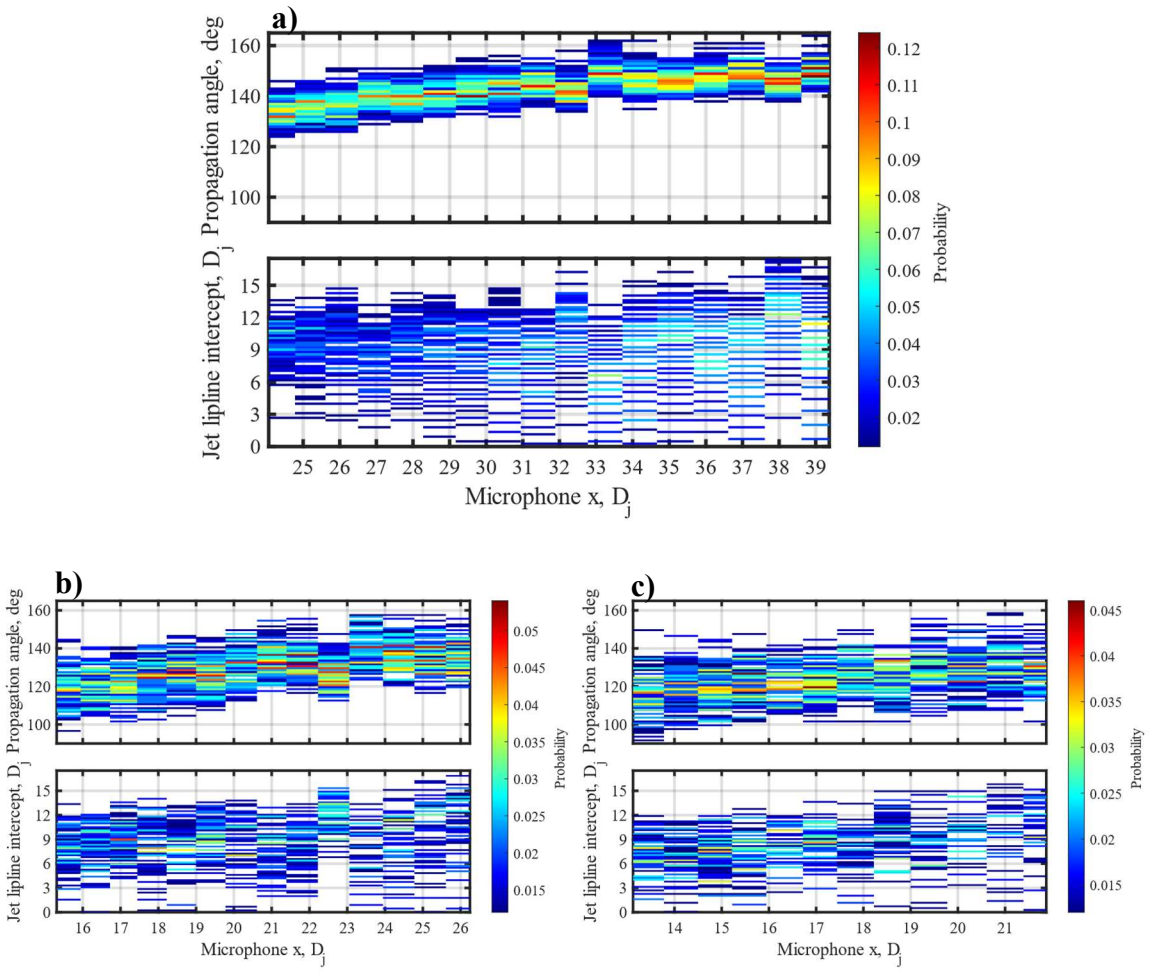

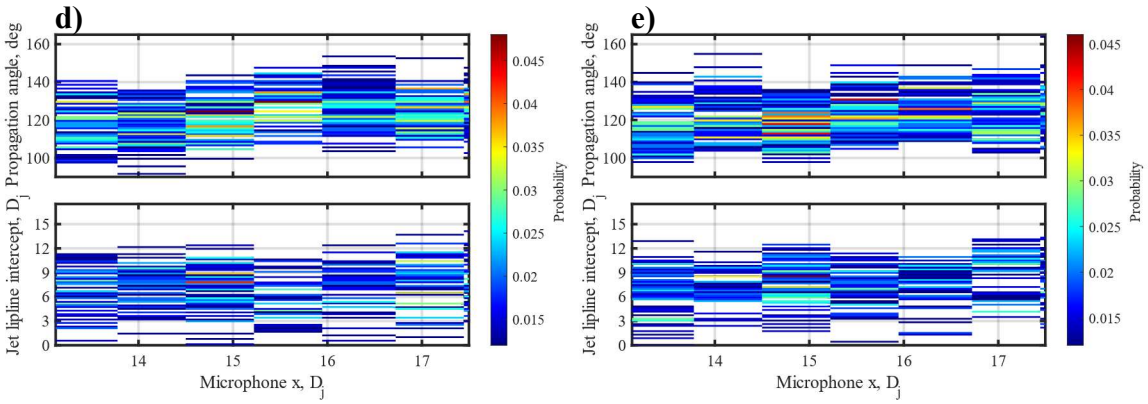

Figure 5. Normalized histograms for each of the five lobes with (a) lobe 1, Sr = 0.07 (b) lobe 2, Sr = 0.15 (c) lobe 3, Sr = 0.24 (d) lobe 4, Sr = 0.31, and (e) lobe 5, Sr = 0.39. Calculated propagation angles are shown in the top part of each subfigure and the corresponding apparent lipline intercepts in the bottom. Color bars are included to indicate the relative probability of an event satisfying that propagation angle/intercept.

Qualitatively, these plots show the typical angular directivity of each lobe as well as the spread of the source region. These approximate results are summarized in Table 2. It should be noted that these values are visually taken from Fig. 5 to identify trends, i.e., there have been no rigorous calculations. Even so, these results compare favorably with those predicted by Olaveson et al. [11]. From their ray tracing analysis of steady-state lobe behavior reconstrued from hybrid beamforming, they predicted radiation angles of about 140° for lobe 1, 128° for lobe 2, 125° for lobe 3, and 120° for lobe 4. Note that due to the resolution of their ray tracing method, they were unable to make predictions for lobe 5. Likewise, their predictions for the source location for the lobes exhibited a decreasing behavior that is also seen here. The fact that both methods produce comparable results provides some measure of confidence in these results, particularly since each method works in a different domain. It is important to note that this method does predict the source location for the lobe much closer to the engine nozzle than the hybrid beamforming. The analysis from Olaveson et al. suggests a clear division between lobes 1 and 2, with lobe 1 occurring farther downstream than lobe 1. While this disagreement is being investigated, it is possible that there is a limitation to the methods, or as Leete et al. [9] suggested, the mechanism responsible for lobe 1 may be different from the higher-order lobes.

Lobe	Estimated radiation angle (°)	Estimated source location (D_j)
1	125-150	6-12
2	110-140	6-12
3	100-140	5-10
4	100-140	3-9
5	100-140	3-9

Table 2. Approximate radiation angles and source locations for each spatiospectral lobe as read from Fig. 5. These values are not rigorously calculated but serve as an identification of the general trends predicted by event-based beamforming.

To better visualize the connection between propagation angle and lipline intercept, the results are now presented as a collection of ray-traced events. For each microphone pair, the mean of the corresponding propagation angle distribution is used to ray trace the average event back to the jet lipline. This gives the benefit of being able to visually identify trends connected between the two parameters as well as comparisons between different Strouhal numbers. Figure 6 shows this ray tracing applied to Strouhal numbers corresponding to the spatiospectral lobes. The ray-traced events are shown as different colored lines, one for each lobe, microphones are represented as blue circles and the jet lipline is shown as a dashed grey line. From this figure, it becomes more apparent that each Strouhal number (lobe) originates from near the same location but at a different radiation angle. The implication is then that multiple overlapping sources are producing different Strouhal numbers. Section V.B investigates the differences in event timing.

Leete et al. [28] studied noise radiation properties from a large-eddy simulation (LES) of a highly heated, imperfectly expanded jet performed by Liu et al. [29–31] with parameters defined to mimic the T-7A afterburning conditions. In their analysis, they determined that the potential core tip extends out to roughly 7.2 D_j. Supposing that this value is similarly appropriate for MIL, these results suggest that the events corresponding to lobes 2 and 3

(St = 0.15 and 0.24) are occurring right around the potential core tip. Additionally, lobes 4 and 5 (St = 0.31 and 0.39) are occurring slightly upstream of the potential core tip.

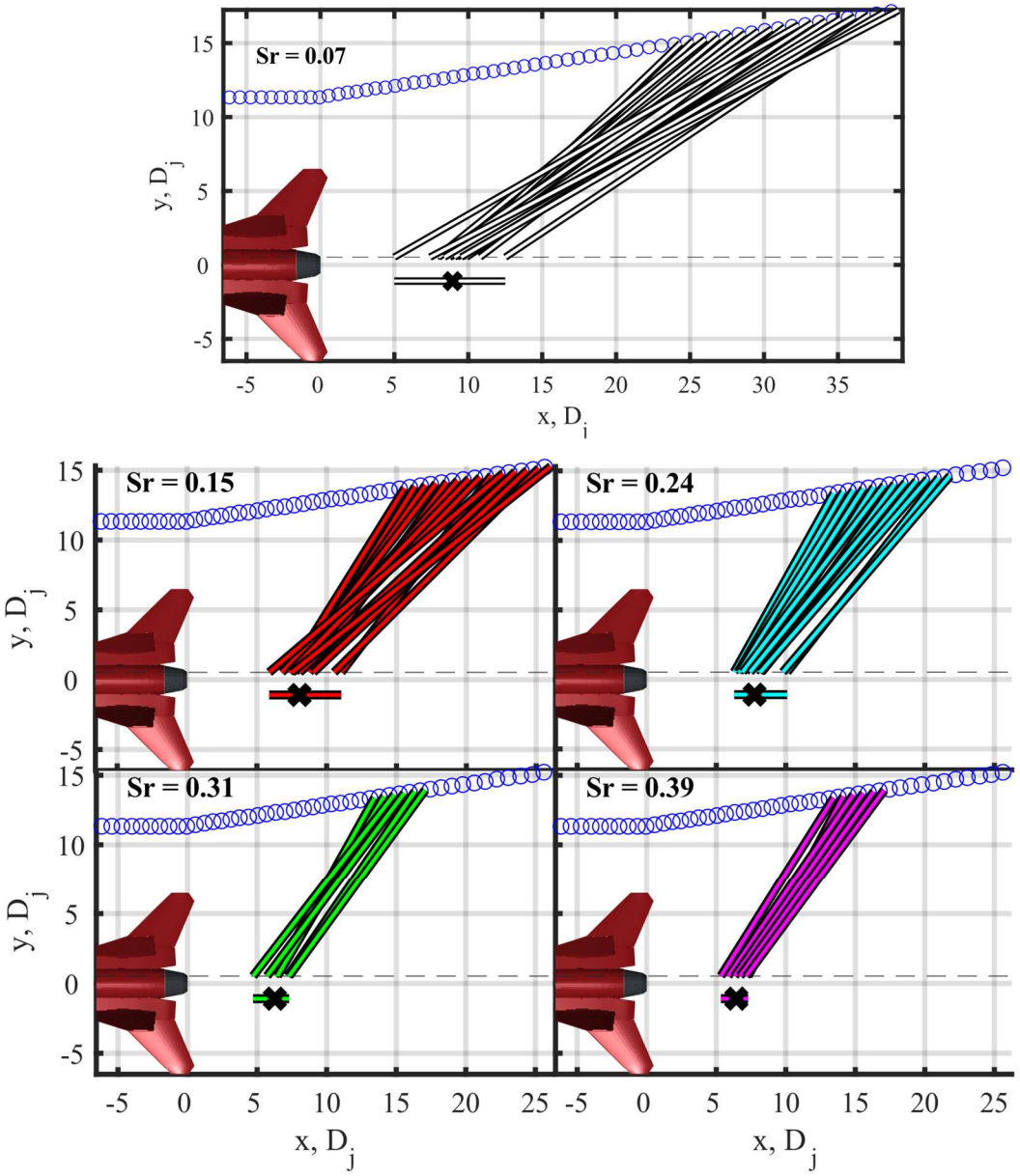

Figure 6. Ray tracing using the mean of the propagation angle distribution for five Strouhal numbers corresponding to the spatiospectral lobes. Included beneath the x-axis in each figure is a bar indicating the range of the traced intercept distribution with the mean intercept being represented with an X. Note that while each group has a different radiation angle, their apparent lipline source locations have notable overlap.

B. Time-Frequency Event Characterization

While the events in the previous section are determined uniquely for each frequency, it is also beneficial to consider the events in a time-frequency sense. In the previous section events from only a single frequency are used, but inspection of Fig. 4 suggests that the high amplitude events in $|W_x|^2$ extend across frequency and not only time. Thus, a single-frequency analysis will be unable to capture all the pertinent details.

The waveform from Fig. 4 exhibits multilobed behavior. The left plot in Fig. 7 shows the autospectral density of the full 30-second waveform using a frequency bin size of 10 Hz (ΔSr $\approx$ 0.005). This spectrum has two notable peaks at Strouhal numbers of 0.14 and 0.24 and a prominent dip at 0.20. The peaks indicate that these are the most prominent

Strouhal numbers in the signal and correspond to the spatiospectral lobes appearing at that microphone location. Since the lobes change in frequency, this microphone has a peak at Sr = 0.14 instead of the 0.15 analyzed in the preceding analysis. The next step is to analyze this spectral content in the time domain. The right of Fig. 7 shows $|W_x|^2$ for a 30 ms portion of the waveform. This segment was chosen due to the larger number of events, seen as local maxima. Included in the figure are three horizontal lines. The green lines highlight the autospectral peaks while the magenta line shows the location of the dip. A preliminary observation shows that many of the events coincide with one of these peak frequencies. It is also to be noted that there are many events above the 410 Hz line. These correspond to the other minor spectral peaks, and it is expected that a peak in the spectrum correlates to high amplitude events at that Strouhal number. Additionally, there are several events seen to appear at the spectral dip. This is not unexpected. While there is a local minimum at a Strouhal number of 0.20, this level is still higher than much of the spectrum and would imply the presence of an increased amplitude at this frequency.

A feature of interest in Fig. 7 is the relation between the events at each Strouhal number of interest. Between Fig. 7 and observations in other time snapshots, events appear to oscillate between the spectral peaks. This behavior is most notable around 1.95 s where four events bounce back and forth between the two green lines and then a fifth on the magenta line. It is observed that this oscillatory behavior is not periodic, and neither is the spacing between these groups of events. It is also noted that whenever there is an event at one of the peak frequencies, there tends to be a relative minimum at the other peak. This behavior suggests that the events are not generated simultaneously in time. This pattern has some semblance to the modal switching observed by Heeb et al. [21] who used wavelets to study modal switching in screech tones of a lab-scale jet.

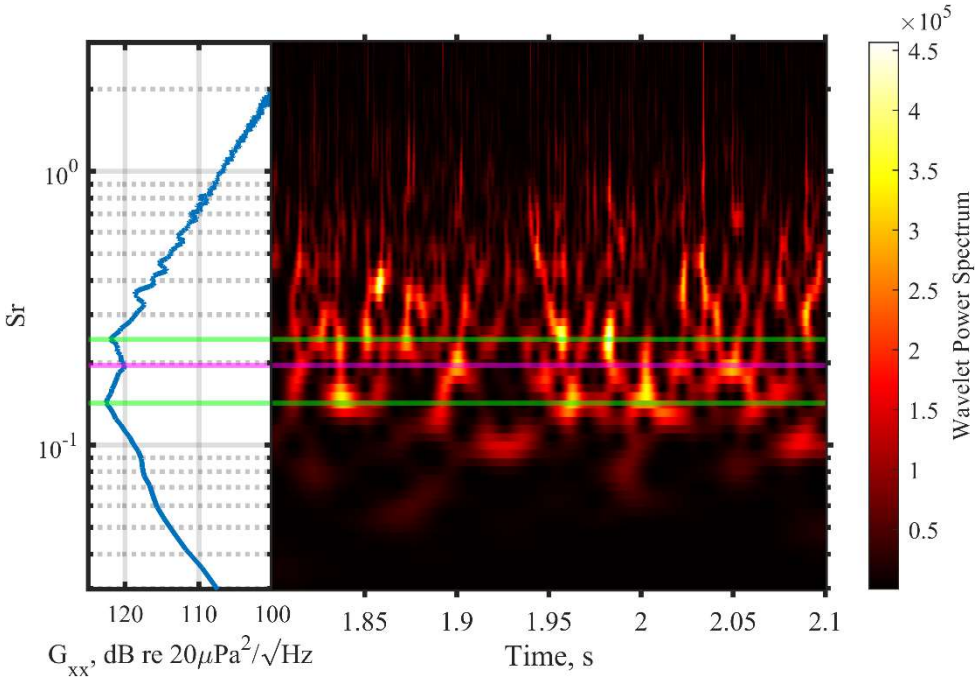

Figure 7. Autospectral density (left) of the full 30-sec waveform from Fig. 4 demonstrating a double peak and the wavelet transform (right) of a 20 ms windows centered at 1.95 s. Horizontal lines identify extrema locations, with green representing peaks Strouhal numbers of 0.14 and 0.24 and magenta at the central dip at 0.20.

It is critical to verify that this temporal frequency-switching behavior is physical. To do this, wavelet power spectrum frequency slices for the spectral peaks are compared. First, the top 500 high-amplitude events are defined in $|W_x(0.14,t)|^2$ using the same method as in EBBF. Each event is then divided by the corresponding time location in $|W_x(0.24,t)|^2$ and then converted to a decibel quantity to amplify the low-value behavior. Mathematically this is calculated as

$$R_1 = 10\,log_{10}\left(\frac{|W_x(0.14,t_1)|^2}{|W_x(0.24,t_1)|^2}\right) \tag{3}$$

where t_1 is the time location of the 500 events in $|W_x(0.14, t)|^2$. The process is then repeated for the Sr = 0.24 slice, compared to the Sr = 0.14 slice, and is shown as

$$R_2 = 10\, log_{10}\left(\frac{|W_x(0.24, t_2)|^2}{|W_x(0.14, t_2)|^2}\right) \tag{4}$$

where t_2 is the time location of the 500 events in $|W_x(0.24, t)|^2$. These two functions are then plotted as a histogram to show the general distribution.

Figure 8 shows the two histograms over a 20 dB range with the mean value included in the title. The left plot shows R_1 and R_2 on the right. The mean of R_1 is 5.6 dB and the mean of R_2 is 9.0 dB. This means that for each identified event at Sr = 0.14, the corresponding value at Sr = 0.24 is on average 5.6 dB lower. If it were coincidental that an observed maximum at one peak coincided with a null at the other peak, there would be cases where an event at one Strouhal number corresponds with an event at the other. Since these two signals have relatively equal time-averaged amplitude, this would cause the distribution to trend towards a Gaussian with a mean of 0 dB. The nonzero means imply some sort of switching phenomenon occurring.

Statistically, it is possible that these distributions have a mean of zero and the events selected here represent a skewed sampling. To test this possibility, a t-test can be used. In brief, the t-test compares two sample distributions and determines how likely it is that they come from the same parent distribution. When performed on a single distribution, such as R_1, the test shows how likely it is that the true mean is zero and provides a confidence interval for the location of the true mean. If the mean confidence interval overlaps with zero, it is not statistically different from a distribution with a mean of zero. The results from the t-test provide a 95% confidence interval of 5.1- 6.1 dB for R_1 and 8.5-9.4 dB for R_2. The t-test reports the probability that the actual mean is zero is on the order of 10^{-80}, which is so small as to be impossible. Thus, statistically, these distributions provide evidence that events are not occurring at the same instant in time. Between visual observations and this statistical analysis, the phenomenon qualitatively resembles the mode switching seen in jet screech. The next section investigates this possibility further.

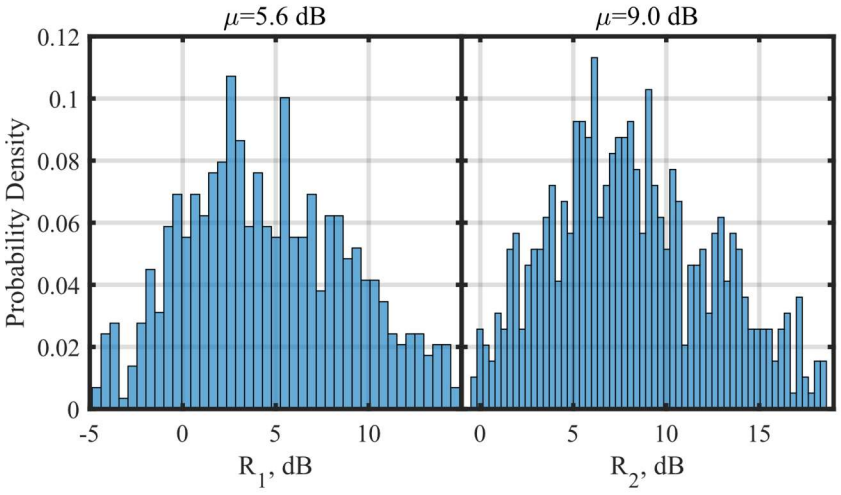

Figure 8. Histograms comparing the wavelet magnitude at 500 events along the Sr = 0.14 and 0.24 wavelet power spectrum slices. A value of zero indicates that the two slices have the same magnitude at the event location.

C. Markov Chains

Markov chains can be used to describe a system that randomly switches between multiple states under the condition that the next state only depends on the current one. These types of Markov models were first applied to the analysis of letter content in poetry [32]. Other applications have been in communication and information theory [33], the response time of shared computational resources [34], gene identification on DNA strands [35], and speech recognition [36].

A Markov chain describes a sequence of time-evolving states under the condition that the next state only depends on the current value of the chain. A simple computational example is Euler's method: $y(t_{n+1}) = y(t_n) + \Delta t \frac{dy}{dt}|_{t=t_n}$ assuming that $\frac{dy}{dt}$ is provided externally as is the case with an initial value problem. In this scheme, the t_{n+1} term is calculated only using the information at t_n. Thus, the sequence will evolve according to the derivative and the current time step. Other schemes, like Runge-Kutta, may use previous time steps for better convergence or derivative calculations. These methods are distinctly not Markovian. Most applications of the Markov chain occur outside of computational methods.

The basic Markov analysis is best suited for a system with a finite number of states, such as those in probability analysis. One such example is a taxi driver that works between three cities: A, B, and C. Suppose that as the driver collects and deposits passengers, they record the letter of the city where they drop off passengers. Perhaps most people have local destinations and only a few are traveling outside of their current city. In these cases, the driver is more likely to remain in one place for a longer time and their city 'state sequence' will be characterized by long strings of repeated letters. Now suppose that the only nearby airport is in city A. This will cause more people to travel to city A. Now, whenever the driver finds themselves in city B or C, they will be more likely to transition to city A. These underlying structures can frequently be conveyed by a probability transition matrix *T* composed of matrix elements T_{ij} that indicate the probability of transitioning from state *i* to *j*. It is important to note that the transition matrix is row normalized, if not the system would not be closed or physical. In the example of the taxi driver, when most people stay local, the diagonal elements will become larger. When the only airport is in city A, the elements T_{BA} and T_{CA} will also increase. It is important to note that for a truely random process, each matrix element will be identical.

The remainder of this section details the process of applying the Markov chain to the frequency-switching phenomenon observed in section V.B. To generate a transition matrix that models the frequency-switching behavior, the first step is to procure a state sequence. Since the events in the wavelet transform appear at the important locations of the corresponding spectrum, only these two Strouhal numbers will be considered. The state sequence is then generated from the wavelet transform as follows.

First, the $|W_x(0.14, t)|^2$ Strouhal number slice is extracted from the wavelet transform and divided into six thousand 5 ms blocks. This block size was chosen to match the observation that many events have a duration on the order of about 15 ms. The Markov chain should have a step size on the order of the modeled events. If the step size is too large, the chain will not be able to accurately capture individual events. If the step size is too small, the diagonal terms of the transition matrix become large relative to the off-diagonals and the resultant matrix approaches the identity. Thus, a step size on the order of the events will capture the underlying event structure while also producing a more readable transition matrix. It is to be noted that a smaller step size does produce the same results and is used later in this section, but it is difficult to interpret a matrix whose off diagonals are vanishingly small. Once the signal has been divided into blocks, the average value of each block is compared to the rms value of the wavelet slice. If the block mean is larger than the rms value, then that sample is marked as having an event at Sr = 0.14. This same procedure is then repeated for Sr = 0.24. Once both sequences have been created, each sample is compared and a final state sequence is created. States are defined as: S_{10} for an event only at Sr = 0.14, S_{01} for an event only at Sr = 0.24, S_{00} when no events are present and S_{11} when an event is present at both frequencies. The inclusion of S_{11} is to allow for those cases when there is an overlap between events as well.

Once the state sequence is defined, MATLAB's *hmmestimate* function is used to fill out the transition matrix. These values are presented in Table 3 with labels included for simpler interpretation. The table can be read by starting at any of the four states in the left-hand column. Then, the probability of transitioning to any of the other states is identified by finding the column corresponding to the desired state. From this matrix, there are a few observations to be made. Firstly, the relative duration of a state is related to the probability of a state transitioning to itself. This indicates that events at Sr = 0.14 are generally longer than those at Sr = 0.24 which in turn are larger than the overlap between the two. Additionally, it is observed that gaps between states tend to be larger than each state individually.

It is also beneficial to consider the long-term, or steady-state solution predicted by the transition matrix. This is calculated as $\lim_{n\to\infty} T^n$. In words, it is the probability of transitioning from one state to another after *n* time steps. As *n* goes to infinity, each row becomes identical and the result is a description of the overall state content of the system [37]. From the bottom row of Table 3, it is observed that a majority of the signal is dominated by an absence of events at these Strouhal numbers. More important though is the result that events are six times more likely to occur at either of the peak Strouhal numbers than at both simultaneously. This confirms the statistical analysis presented in Fig. 8 that it is more likely for events to occur at different instances in time. Combining this with the observation from Fig. 6 that high-amplitude spectral events have different directivities, the result is a rapid directivity switching occurring on the time scale of the average gap duration between events. This seems then to suggest that the turbulent events

corresponding to the spatiospectral lobes are occurring at different times and that their superposition is an effect of the usual statistically averaged methods such as holography and beamforming.

It is important to point out that this same process has been applied to Gaussian white noise shaped to have the same spectral shape as in Fig. 7. The results are similar to those seen in Table 3. This suggests that the distributions of events along either wavelet slice are independent of each other and follow a random Gaussian distribution.

From\To	S_{00}: Neither	S_{01}: 0.24	S_{10}: 0.14	S_{11}: Both
S_{00}: Neither	0.720	0.148	0.105	0.027
S_{01}: 0.24	0.490	0.341	0.101	0.069
S_{10}: 0.14	0.393	0.080	0.422	0.105
S_{11}: Both	0.257	0.174	0.363	0.206
Steady State	0.597	0.170	0.175	0.058

Table 3. Transition matrix corresponding to the event state sequence extracted from the wavelet transform presented in Fig. 7. Each element represents the probability of making a transition from the row state to the column state at each time step. In addition to the matrix elements, the steady-state solution is also included which represents the long-term state content of the system.

In addition to the transition matrix discussed above, the Markov state sequence is now used to perform an event-based spectral decomposition. To begin, a new state sequence is generated using the same procedure outlined above with the exception that instead of dividing the signal into blocks, each sample of the waveform is used. Using this new state sequence as a guide, the spectrum for each event is extracted from $|W_x|^2$. The average spectrum corresponding to a specific state is then calculated as:

$$G_{xx} = \frac{1}{N}\sum_{i=1}^{N}|W_x(Sr, t_i)|^2 \tag{5}$$

where N is the number of times the state appears in the sequence and subscript i indicates the time location corresponding to that state. In addition to each event spectrum, the average spectrum is included. These curves are plotted in Fig. 9 along with the time-averaged autospectral density as shown in Fig. 7. It is first seen that the mean wavelet spectrum closely matches the Fourier spectrum. There is, however, some notable smoothing caused by the wavelet transform. This is to be expected since the Morlet wavelet has a broader spectral response than the complex exponential used in the Fourier transform. It would be expected that using a different wavelet would similarly impact the shape of the averaged spectrum. From Fig. 9 it is observed that when events occur at only a single frequency, there is a reduction of energy at the other frequency. This again supports the statistical analysis from Fig. 8: events at one Strouhal number are occurring at nulls relative to the other. This has the effect of showing that individual peaks in the spectrum are caused by localized events at the corresponding Strouhal number.

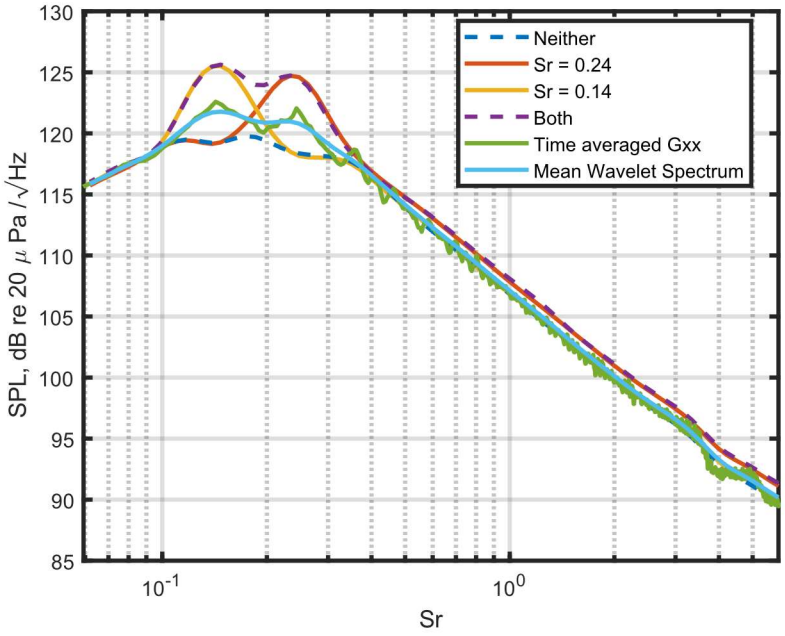

Figure 9. Event-based spectral decomposition using events from the wavelet transform and state assignment from the Markov chain.

VI. Conclusion

This paper investigated the temporal characteristics of the spatiospectral lobes using a joint time-frequency domain approach. The event-based beamforming algorithm developed in a previous crackle study was implemented for the T-7A. The wavelet transform was then used to extract spectral information as a function of time. By using the wavelet transform in conjunction with the event-based beamforming, spectral events corresponding to the spatiospectral lobe Strouhal numbers were ray traced from the microphone array to the jet lipline. It was found that individual lobes appear to the radiating from similar source locations but at different directivities. Using the wavelet transform, the spatiotemporal structure was characterized for a single microphone signal. This signal exhibits a dual-peaked spectrum. Visual and statistical analysis suggested a spectral switching behavior between the two prominent Strouhal numbers similar to the mode switching of lab-scale jet screech. A Markov-style analysis was then used to model the distribution of events along the two Strouhal numbers. It was found that while events at one spectral peak do not exclude events at the other, the distributions favor spectral events separated in time. Since the event-based beamforming predicts different directivities for different Strouhal numbers, it appears that the sound radiated from the jet has rapid and discrete directivity changes.

Future investigation will include exploring the benefits of using different wavelets in the analysis. The Markov-style analysis will also be applied to the entire microphone array to further characterize the temporal behavior of the other spatiospectral lobes. From these results, the event-based spectral decomposition will be applied to the spatiospectral plots to determine the broader behavior of the individual lobes.

VII. Acknowledgments

This work is funded by ONR grant number N00014-21-1-2069 titled “Connecting analyses of installed tactical jet engine noise with simulated and laboratory-scale data,” with project monitor Dr. Steven Martens (Code 351 Jet Noise Reduction). Distribution A: Approved for public release; distribution unlimited. Cleared 05/12/2023.

VIII. References

[1] Martens, S., and Spyropoulos, J. T. *Practical Jet Noise Reduction for Tactical Aircraft*. 2010.

[2] Wall, A. T., Gee, K. L., Neilsen, T. B., McKinley, R. L., and James, M. M. “Military Jet Noise Source Imaging Using Multisource Statistically Optimized Near-Field Acoustical Holography.” *The Journal of the Acoustical Society of America*, Vol. 139, No. 4, 2016, pp. 1938–1950. https://doi.org/10.1121/1.4945719.

[3] Wall, A. T., Gee, K. L., Neilsen, T. B., Harker, B. M., McInerny, S. A., McKinley, R. L., and James, M. M. "Investigation of

Multi-Lobed Fighter Jet Noise Sources Using Acoustical Holography and Partial Field Decomposition Methods". *21st AIAA/CEAS Aeroacoustics Conference*, paper number 2015-2379, 2016.
[4] Neilsen, T. B., Gee, K. L., Wall, A. T., and James, M. M. "Similarity Spectra Analysis of High-Performance Jet Aircraft Noise." *The Journal of the Acoustical Society of America*, Vol. 133, No. 4, 2013, pp. 2116–2125. https://doi.org/10.1121/1.4792360.
[5] Harker, B. M., Neilsen, T. B., Gee, K. L., Wall, A. T., and James, M. M. "Spatiotemporal-Correlation Analysis of Jet Noise from a High-Performance Military Aircraft" *AIAA Journal*, paper number 2015-2376, 2015.
[6] Tam, C. K. W., and Parrish, S. A. "Noise of High-Performance Aircraft at Afterburner." *Journal of Sound and Vibration*, Vol. 352, 2015, pp. 103–128. https://doi.org/10.1016/j.jsv.2015.04.010.
[7] Stout, T. A., Gee, K. L., Neilsen, T. B., Wall, A. T., and James, M. M. "Acoustic Intensity near a High-Powered Military Jet Aircraft." *The Journal of the Acoustical Society of America*, Vol. 138, No. 1, 2015, pp. EL1–EL7. https://doi.org/10.1121/1.4921746.
[8] Swift, S. H., Gee, K. L., Neilsen, T. B., Wall, A. T., Downing, J. M., and James, M. M. "Spatiotemporal Correlation Analysis of Jet Noise from a Round-Nozzle Supersonic Aircraft." *2018 AIAA/CEAS Aeroacoustics Conference*, paper number 2018-3938, 2018.
[9] Leete, K. M., Wall, A. T., Gee, K. L., Neilsen, T. B., James, M. M., and Downing, J. M. "Acoustical Holography-Based Analysis of Spatiospectral Lobes in High-Performance Aircraft Jet Noise." *AIAA Journal*, paper number 2018-2826, 2018.
[10] Stout, T. A., Gee, K. L., Neilsen, T. B., Wall, A. T., and James, M. M. "Source Characterization of Full-Scale Jet Noise Using Acoustic Intensity". *Institute of Noise Control Engineering.* 2015.
[11] Olaveson, T., Ward, J., Johnson, J., Gee, K. L., and Wall, A. T. "Analysis of Spatiospectral Lobes in Installed F404 Engine Noise Radiation." *28th AIAA/CEAS Aeroacoustics 2022 Conference*, paper number 2022-3087, 2022.
[12] Padois, T., Gauthier, P. A., and Berry, A. "Inverse Problem with Beamforming Regularization Matrix Applied to Sound Source Localization in Closed Wind-Tunnel Using Microphone Array." *Journal of Sound and Vibration*, Vol. 333, No. 25, 2014, pp. 6858–6868. https://doi.org/10.1016/j.jsv.2014.07.028.
[13] Mathews, L. T., Gee, K. L., Leete, K. M., and Wall, A. T. "Acoustic Source Characterization of an Installed GE F404 Engine Using Near-Field Acoustical Holography." *28th AIAA/CEAS Aeroacoustics 2022 Conference*, paper number 2022-3028, 2022.
[14] Oertel Sen, H., Seiler, F., Srulijes, J., and Hruschka, R. "Mach Waves Produced in the Supersonic Jet Mixing Layer by Shock/Vortex Interaction." *Shock Waves*, Vol. 26, No. 3, 2016, pp. 231–240. https://doi.org/10.1007/s00193-015-0612-1.
[15] Akamine, M., Okamoto, K., Teramoto, S., and Tsutsumi, S. "Conditional Sampling Analysis of High-Speed Schlieren Movies of Mach Wave Radiation in a Supersonic Jet." *The Journal of the Acoustical Society of America*, Vol. 145, No. 1, 2019, pp. EL122–EL128. https://doi.org/10.1121/1.5088493.
[16] Vaughn, A. B., Neilsen, T. B., Gee, K. L., Wall, A. T., Micah Downing, J., and James, M. M. "Broadband Shock-Associated Noise from a High-Performance Military Aircraft." *The Journal of the Acoustical Society of America*, Vol. 144, No. 3, 2018, pp. EL242–EL247. https://doi.org/10.1121/1.5055392.
[17] Vaughn, A. B., Gee, K. L., Swift, S. H., Leete, K. M., Wall, A. T., Downing, J. M., and James, M. M. "Source Localization of Crackle-Related Events in Military Aircraft Jet Noise." *AIAA Journal*, paper number 2019-2664, 2019
[18] Vaughn, A. B., Gee, K. L., Swift, S. H., Wall, A. T., Downing, J. M., and James, M. M. "Beamforming of Supersonic Jet Noise for Crackle-Related Events." *Proceedings of Meetings on Acoustics,* Vol. 040003, 2019, p. 040003. https://doi.org/10.1121/2.0000998.
[19] Torrence, C., and Compo, G. P. "A Practical Guide to Wavelet Analysis." *Bulletin of the American Meteorological Society*, Vol. 79, No. 1, 1998, pp. 61–78. https://doi.org/10.1175/1520-0477(1998)079<0061:APGTWA>2.0.CO;2.
[20] Baars, W. J., and Tinney, C. E. "Shock-Structures in the Acoustic Field of a Mach 3 Jet with Crackle." *Journal of Sound and Vibration*, Vol. 333, No. 12, 2014, pp. 2539–2553. https://doi.org/10.1016/j.jsv.2014.01.008.
[21] Heeb, N., Mora, P., Kastner, J., Gutmark, E., Kailasanath, K., and Liu, J. "Mode Switching of Jet Noise Screech." *18th AIAA/CEAS Aeroacoustics Conference*, paper number 2012-2162, 2012.
[22] Leete, K. M., Vaughn, A. B., Bassett, M. S., Rasband, R. D., Novakovich, D. J., Gee, K. L., Campbell, S. C., Mobley, F. S., and Wall, A. T. "Jet Noise Measurements of an Installed Ge F404 Engine". *AIAA Scitech 2021 Forum*, paper number 2021-1638, 2021.
[23] Vaughn, A. B., Gee, K. L., Swift, S. H., Leete, K. M., Wall, A. T., Downing, J. M., and James, M. M. "Crackle-Related Beamforming of Military Jet Aircraft Noise". *25th AIAA/CEAS Aeroacoustics Conference*, paper number 2019-2664, 2019.
[24] Russavage, P. B., Neilsen, T. B., Gee, K. L., and Hales Swift, S. "Rating the Perception of Jet Noise Crackle." *Proceedings of Meetings on Acoustics*, Vol. 33, No. 1, 2018. https://doi.org/10.1121/2.0000821.
[25] Baars, W. J., Tinney, C. E., Wochner, M. S., and Hamilton, M. F. "On Cumulative Nonlinear Acoustic Waveform Distortions from High-Speed Jets." *Journal of Fluid Mechanics*, Vol. 749, 2014, pp. 331–366. https://doi.org/10.1017/jfm.2014.228.
[26] Bendat, J. S., and Piersol, A. G. *Random Data.* 1987.
[27] Reichman, B. O., Gee, K. L., Neilsen, T. B., Swift, S. H., Wall, A. T., Downing, J. M., and James, M. M. "Acoustic Shock Formation in Noise Propagation During Military Aircraft Ground Run-Up Operations." *AIAA Journal*, paper number2017-4043, 2022.
[28] Leete, K. M., Gee, K. L., Liu, J., and Wall, A. T. "Coherence Analysis of the Noise from a Simulated Highly Heated Laboratory-Scale Jet." *AIAA Journal*, paper number2019-2633, 2020.
[29] Liu, J., Kailasanath, K., and Gutmark, E. J. "Similarity Spectra Analysis in Highly Heated Supersonic Jets Using Large-Eddy

Simulations". *55th AIAA Aerospace Sciences Meeting*, paper number 2017-0926 2017.
[30] Liu, J., Corrigan, A., Kailasanath, K., and Gutmark, E. "Impact of Chevrons on Noise Source Characteristics in Imperfectly Expanded Jet Flows". *21st AIAA/CEAS Aeroacoustics Conference*, paper number 2015-2835, 2015.
[31] Liu, J., Corrigan, A., Kailasanath, K., and Taylor, B. "Impact of the Specific Heat Ratio on the Noise Generation in a High-Temperature Supersonic Jet". *54th AIAA Aerospace Sciences Meeting*, paper number 2016-2125, 2016.
[32] Hilgers, P. Von, and Langville, A. . "The Five Greatest Applications of Markov Chains." *Proceedings of the Markov Anniversary meeting*, 2006, pp. 155–168.
[33] Shannon, C. E. "A Mathematical Theory of Communication." *Bell System Technical Journal*, Vol. 27, No. 3, 1948, pp. 379–423. https://doi.org/10.1002/j.1538-7305.1948.tb01338.x.
[34] Frenkel, A. K. A. "Allan L . Sherr : Big Blue's Time-Sharing Pioneer." 1987.
[35] Henderson, J. "Finding Genes in DNA with a Hidden Markov Model." *Journal of Computational Biology*, Vol. 4, No. 2, 1997, pp. 127–141. https://doi.org/10.1089/cmb.1997.4.127.
[36] Bahl, L. R., Jelinek, F., and Mercer, R. L. "A Maximum Likelihood Approach to Continuous Speech Recognition." *IEEE Transactions on Pattern Analysis and Machine Intelligence*, Vol. PAMI-5, No. 2, 1983, pp. 179–190. https://doi.org/10.1109/TPAMI.1983.4767370.
[37] Meyn, S. P., and Tweedie, R. L. *Markov Chains and Stochastic Stability*. 2005.